Hindawi
Advances in Materials Science and Engineering
Volume 2022, Article ID 4498458, 14 pages
https://doi.org/10.1155/2022/4498458

Research Article

A New Stress Monitoring Method for Mechanical State of Buried Steel Pipelines under Geological Hazards

Xinze Li,[1,2,4] **Qingbai Wu**,[1,2] **Huijun Jin**,[1,2,3] **and Wei Kan**[5]

[1]*State Key Laboratory of Frozen Soils Engineering, Northwest Institute of Eco-Environment and Resources, Chinese Academy of Sciences, Lanzhou 730000, China*
[2]*School of Resources and Environment, University of Chinese Academy of Sciences, Beijing 100049, China*
[3]*Northeast-China Observatory and Research-Station of Permafrost Geo-Environment (Ministry of Education), Institute of Cold-Regions Science and Engineering, School of Civil Engineering, Northeast Forestry University, Harbin 150040, China*
[4]*Department of Chemical and Material Engineering, University of Alberta, Edmonton, AB T6G 1H9, Canada*
[5]*Dragon Resources Company, Beijing 100049, China*

Correspondence should be addressed to Xinze Li; xinze4@ualberta.ca

Received 19 December 2021; Revised 2 February 2022; Accepted 5 February 2022; Published 24 March 2022

Academic Editor: Francesco Colangelo

Long-distance pipelines are threatened by a variety of natural geological hazards. A stress monitoring system driven by the strain-stress solution algorithm was proposed; it can achieve real-time maximum axial stress measurement by installing vibrating wire gauges (VWGs) on the surface of the pipe. To verify the effectiveness of the algorithm, a large-scale pipe mechanical loading experiment combined with a finite element model (FEM) was conducted. The results show that VWGs were reliable with a relative error of 1.19%~7.98% compared with resistance strain gauges (SGs). The FEM was also reliable with a maximum relative error of 4.04% compared with theoretical analysis. When the reasonable combination modes of VWGs were chosen utilizing the least square method, the error of the pipe stress detection algorithm could be controlled within the range of −13.33~16.66%. This pipeline stress monitoring technology can meet the requirement of 24-hour dynamic monitoring of the underground pipeline's mechanical state, realizing the early warning of geohazards.

1. Introduction

1.1. Background. Pipelines are key elements of the energy supply chain. The geological conditions along the long-distance oil and gas pipeline are complicated, and the pipelines are subjected to geological hazards with high risks such as landslide, fault, earthquake, and permafrost [1, 2]. The geological hazards may result in pipeline deformation, stress concentration, upheaval buckling, creep, and even rupture which seriously threaten the structural integrity and long-term safe operation of the pipeline [3]. Although the types of geological hazards are different, the impact of natural geohazards on the pipeline is ultimately reflected in the mechanical state and bearing capacity of the pipeline. If the excessive load applied to a pipeline exceeds the pipeline limit, the pipeline may fail. In addition, even though stress concentration is within the pipeline limit, accidents may also occur if extra control or elimination measures are not taken.

The pipe's stress and strain responses under various kinds of loads can be investigated through analysis of pipe-soil interactions. From the perspective of soil, as a kind of granular material, the soil has complex mechanical properties due to involved physical and chemical processes [4–6]. Many types of constitutive models including the elastoplastic model, superplastic model, and thermo-hydro-mechanical (THM) model were developed to investigate the behaviors of various types of soil such as loess, freezing soil, and saline soil. In recent years, the thermodynamic theory was applied in the development of constitutive models [7]. Differing from the critical state soil mechanics theory, some concepts

such as the flow rule, yield function, dissipation potential function, and hardening criterion included in the classical elastoplastic model can be avoided. New concepts of particle entropy, particle temperature, migration coefficient, and potential energy density function were introduced [8]. Bai et al. [9] proposed a new coupled THM model established under the framework of granular thermodynamics. The influencing factors such as the temperature, saturation, microstructure of the soil skeleton, and phase transition between the liquid and solid/gas phases were reflected in the model. Differing from the classical effective principle based on linear elastic porous media, a generalized effective principle considering the impact of the stress path, temperature path, and soil structure was derived.

From the perspective of the pipeline itself, there are two pipe strength-checking methods based on stress or strain presented in pipeline design standards. The stress-based design criteria are based on limit stress criteria, which ensure that the pipe stress or equivalent stress generated by an external load is less than the minimum yield stress (SMYS) of the pipe itself [10]. The strain-based design criteria are based on limit state design and displacement-control load, which allow that pipeline strain to exceed the specified yield strain resulting in plastic deformation occurring in the pipeline; however, the pipeline still meets the operation requirements [11].

The pipeline strain induced by deformation is a direct reflection of the mechanical state of the pipeline [12]. Commonly pipeline strain is monitored to calculate the pipe's stress component which is the most intuitive parameter to examine the safety and stability state of the pipeline [13, 14]. The high-precision measurement of strain value during pipeline operation will be crucial to its strength checking and safety assessment [15]. Because of a characteristic of concealment and temporal hysteresis in the response of pipeline foundation soils to external disturbance, no matter how many considerations have been made in the engineering design stage, it is still impossible to accurately predict all the complex and changeable engineering geological conditions. There will still be great uncertainties and safety risks in the pipeline operation. However, most pipeline accidents attributed to geological hazards have a gradient process in the accumulation of pipe strain and stress, which gives us the possibility of identifying the risk in the early stage and adopting prevention and mitigation measures promptly. Thus, a comprehensive stress monitoring system is required and mandatory, which could make deformation measurements sufficiently sensitive and prompt the detection of the approach to operational tolerance limits.

Monitoring of structural response under various loading conditions has been applied in other geotechnical engineering fields, such as the monitoring of slope, pile structure, tunnel, and dam. Inadequate parameters may lead to uneconomical or sometimes faulty design. Therefore, the application of performance monitoring systems to engineering promotes the transformation from code-based design to performance-based design. Suhail et al. [16] summarized the application of fiber-optic sensor (FOS) technology in monitoring pile performance including pile-soil friction distributions, strain variation with depth, and load transfer behavior. The advantages of FOSs, such as high accuracy, high-temperature durability, and long life cycle, and shortcomings of strain and temperature discrimination were presented. Yuan et al. [17] utilized transparent soil technology combined with particle image velocimetry (PIV) to study the soil deformation processes and displacement trends around a laterally loaded pile. In the experiment, six electrical resistance strain gauges were attached to the model pile body to measure the deformation of the pile. With the rapid development of urbanization, road building and mining have increased the problem of slope stability. Yang et al. [18] summarized the slope deformation monitoring technologies including distributed fiber-optic strain sensor (DFOSS). It is noted that due to the monitoring results being easy to be interfered with by external factors, more studies should be carried out in monitoring data analysis and theoretical models. Some scholars carried out a sensitivity analysis to investigate the effect of influencing factors such as internal friction angle, ratio of the slope, and cohesion on slope stability. The results can provide a reference for the design of the slope and customized slope stability monitoring program. Moreover, postconstruction monitoring and reconnaissance will provide an important feedback loop to the design process [19–21].

Direct monitoring of pipeline strain could be achieved via several technologies. The most notable ones are in-line inspection (ILI), vibrating wire gauges (VWGs), fiber Bragg grating (FBG), and distributed strain sensing (DSS) with fiber optics [22–25]. The ILI tools provide an important means of monitoring pipelines in the permafrost zone, which may experience thaw settlement, frost heave, upheaval buckling buoyancy, and slope instability. For example, the annual ILI tools run over the first 336 km of the Norman Well Pipeline and Trans-Alaska Pipeline System (TAPS) segments in permafrost terrain [26]. A settlement of about 4.57 m at MDX 200 of TAPS was detected using ILI tool [20]. Pipeline bending strain values can be obtained based on the inertial measurement unit (IMU) assembled in the pipeline ILI tool. This technology was employed by the PetroChina Pipeline Company to identify high thawing settlement risk areas along with China-Russia Crude Oil Pipelines (CRCOPs) [27].

Compared with the ILI tool, which provides only a snapshot in time of the strains in the pipeline [28], fiber-optic cable sensor installed along the pipeline and vibrating wire point gauges directly attached to the pipeline could provide strain measurement with a higher frequency. A fiber-optic geotechnical monitoring system has been used on Sakhalin–Khabarovsk–Vladivostok (SKV) gas pipeline, with a total length of approximately 26 km, which crosses 32 Active Tectonic Faults (ATF) in seismically active areas to track pipeline performance. In addition, a total length of 92 km is monitored with strain and temperature fiber-optic sensor cables for ground movement detection [29]. A ground movement monitoring and leak detection system based on fiber-optic monitoring has been applied on the Peru LNG pipeline [30]. The fiber-optic technology can

successfully detect pipeline strain with high accuracy and reliability; however, it is complex and costly from the perspective of installation and data processing. It requires a complex installation geometry that is not paired well with other variables' detection on other abnormal pipeline behavior such as leak detection, ground movement monitoring, and ROW intrusion.

The VWGs could reflect axial strains according to the functional relationship between the vibration frequency of the metal string and the tension force. It has an advantage in reliability compared with SGs, convenient installation compared with FBG or DSS, and high frequency compared with ILI. At the same time, according to the theory of material mechanics and Hooke's Law, the maximum axial stress could be acquired by only knowing three axial strains of the pipe section. Thus, the actual stress and strain variation could be obtained by installing the VWGs on the pipeline monitoring sections. Based on the monitoring results and stress or strain criteria, the degree of pipeline damage caused by geohazards could be evaluated quantitatively, and preventative mitigation measures could be adopted before the pipeline accidents occur. The purpose of this paper is to propose a pipeline stress monitoring system driven by the strain-stress solution algorithm. To verify the effectiveness of the algorithm, a large-scale mechanical loading experiment combined with FEM establishment was carried out for the first time.

1.2. Outline of a Pipe Stress Monitoring System. The pipe stress monitoring system is composed of VWGs, data acquisition controllers, and a monitoring center (Figure 1). The distributed acquisition mode is adopted by arranging main controllers and sensors near the monitoring pipe segments. 3~5 VWGs attached to the pipe section are used to acquire pipe axial strain, and the maximum axial stress could be calculated according to the stress detection algorithm. The data acquisition controllers carry out data acquisition and signal processing. The data is communicated to a PC to reduce the transmission distance of analog quantity and improve the antijamming ability and stability of the whole system. Finally, the stress software installed in the monitoring center performs analysis and early warning realizing the 24-hour monitoring of the pipeline.

2. Materials and Methods

This study facilitates a multisource data coupling analysis for the pipeline's mechanical state (Figure 2): the pipe mechanical loading experiment, the FEM, the algorithm derived, and the basic theory of material mechanics. In particular, it is the first time that the algorithm is published and the pipe mechanical loading experiment for this purpose is carried out.

2.1. Theoretical Basis and Algorithm Derivation. It is assumed that the pipe is in a state of linear elasticity and small deformation. Compared with the inner pressure p and bending moment M, the lateral force Q and torque T are smaller and could be neglected. Therefore, it is considered that all measuring points in the pipe are in a state of bidirectional stress and are only affected by the axial stress σ_L and the hoop stress σ_h. The solution formulas of axial stress σ_L, hoop stress σ_h, and equivalent stress σ are listed as follows. Formula (3) is applicable under the condition that the hoop stress is the first principal stress and the axial stress is the third principal stress (compression).

$$\sigma_L = \sigma \begin{matrix} \max \\ \min \end{matrix}, \tag{1}$$

$$\sigma_L = \frac{p\ D}{2t}, \tag{2}$$

$$\sigma = \sigma_h - \sigma_L. \tag{3}$$

On the monitoring section, 3 VWGs are arranged, and the coordinates of the measuring points are (x_1, y_1), (x_2, y_2), and (x_3, y_3), as depicted in Figure 3. The x axis and y axis define the plane perpendicular to the pipeline axis. The measured axial strains are ε_1, ε_2, and ε_3. The axial force of the pipe is F, and the bending moment is M. The angle between the bending neutral axis x' and the x axis is a.

The projection of bending moment M on x axis and y axis is shown in (4). According to the generalized Hooke Law, the axial strains of the three measuring points are shown in (5).

$$\begin{cases} \mathrm{M}_1 = \mathrm{M}\cos\alpha \\ \mathrm{M}_2 = \mathrm{M}\sin\alpha \end{cases}, \tag{4}$$

$$\begin{cases} \varepsilon_1 = \dfrac{1}{E}\left(\sigma_1 - \mu\dfrac{p\ D}{2t}\right) \\ \varepsilon_2 = \dfrac{1}{E}\left(\sigma_2 - \mu\dfrac{p\ D}{2t}\right), \\ \varepsilon_3 = \dfrac{1}{E}\left(\sigma_3 - \mu\dfrac{p\ D}{2t}\right) \end{cases} \tag{5}$$

where $p\ D/2t$ is the hoop stress (Pa), p is the internal pressure (Pa), D is the outer diameter of the pipe (mm), t is the wall thickness of the pipe (mm), E is the elastic modulus of the pipe (mm), 2.03×10^{11} Pa and μ is Poisson's ratio of the pipe, 0.3.

According to the material mechanics principle, the axial stresses of the three measuring points are shown in the following equation:

$$\begin{cases} \sigma_1 = \dfrac{F}{A} + \dfrac{M_1}{I}y_1 + \dfrac{M_2}{I}x_1, \\ \sigma_2 = \dfrac{F}{A} + \dfrac{M_1}{I}y_2 + \dfrac{M_2}{I}x_2, \\ \sigma_3 = \dfrac{F}{A} + \dfrac{M_1}{I}y_3 + \dfrac{M_2}{I}x_3, \end{cases} \tag{6}$$

where I is the axial moment of inertia of the pipe section (mm^4), $I = \pi/64[D^4 - (D - 2t)^4]$; A is the cross-sectional area of the pipe (mm^2), $A = \pi\ Dt$.

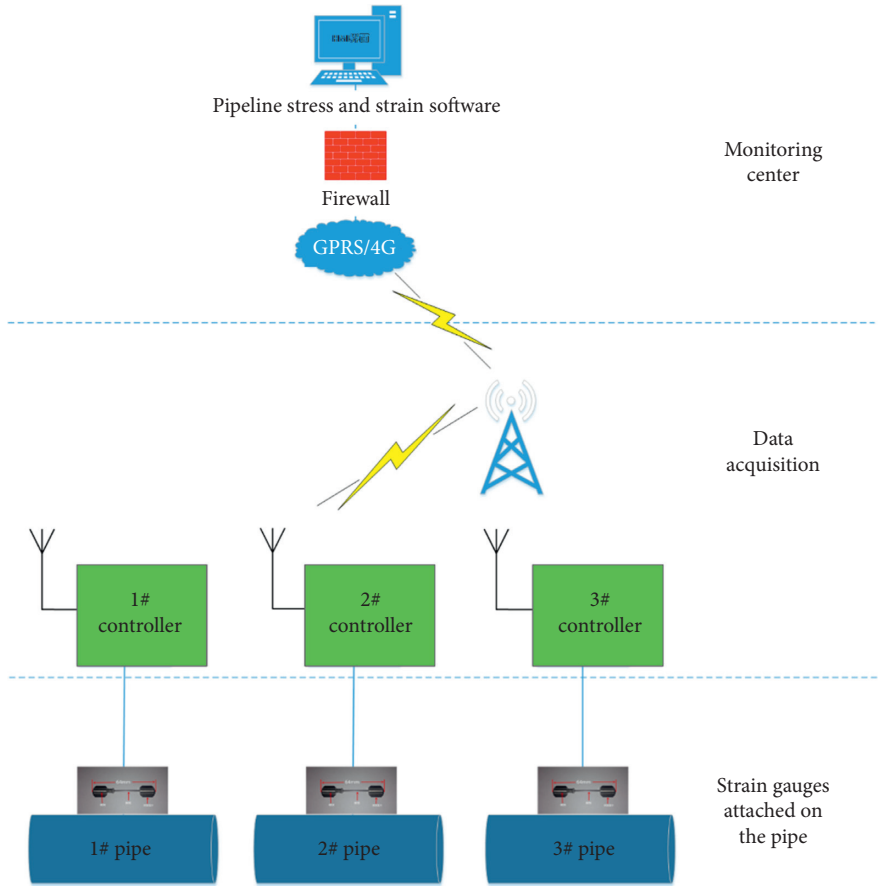

Figure 1: Schematic of pipeline stress monitoring system architecture.

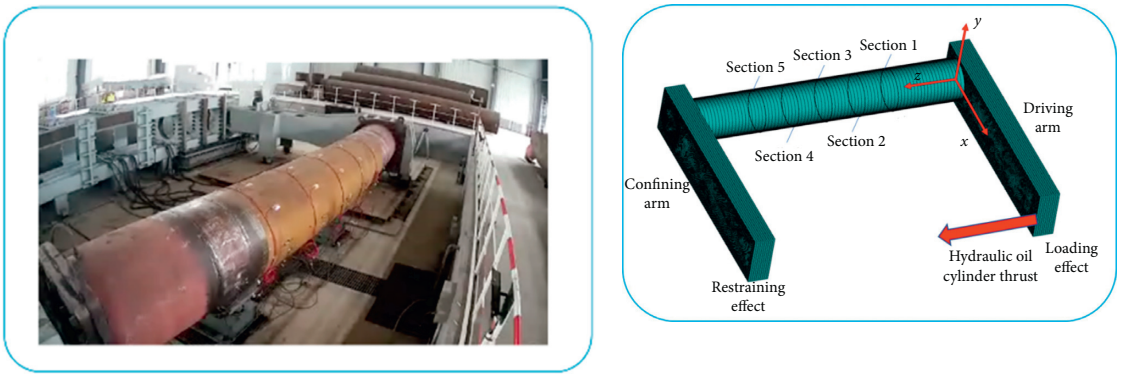

(a) (b)

Figure 2: A large-scale mechanical loading experiment combined with FEM establishment: (a) large-scale mechanical loading experiment; (b) FEM establishment.

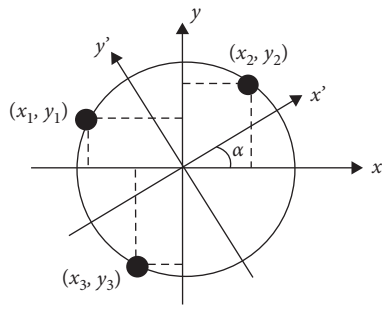

Figure 3: Pipeline cross section with VWGs point sensors.

There are three unknown parameters, F, M_1, and M_2, so three pipe strain measuring points are required. The strains are expressed in the following equations:

$$\varepsilon_1 = \frac{1}{E}\left(\sigma_1 - \mu\frac{P\ D}{2t}\right) = \frac{1}{E}\left(\frac{\mathrm{F}}{A} + \frac{M_1}{I}y_1 + \frac{M_2}{I}x_1\right) - \frac{\mu P\ D}{2Et}, \tag{7}$$

$$\varepsilon_2 = \frac{1}{E}\left(\sigma_2 - \mu\frac{P\ D}{2t}\right) = \frac{1}{E}\left(\frac{F}{A} + \frac{M_1}{I}y_2 + \frac{M_2}{I}x_2\right) - \frac{\mu P\ D}{2Et}, \tag{8}$$

$$\varepsilon_3 = \frac{1}{E}\left(\sigma_3 - \mu\frac{P\ D}{2t}\right) = \frac{1}{E}\left(\frac{F}{A} + \frac{M_1}{I}y_3 + \frac{M_2}{I}x_3\right) - \frac{\mu P\ D}{2Et}. \tag{9}$$

According to the equations above, the maximum and minimum stress and strain can be derived by the following equations:

$$\sigma_{\substack{\max\\\min}} = \frac{F}{A} \pm \frac{M\ D}{2I}, \tag{10}$$

$$\varepsilon_{\substack{\max\\\min}} = \frac{1}{E}\left(\sigma_{\substack{\max\\\min}} - \mu\frac{p\ D}{2t}\right). \tag{11}$$

2.2. Large-Scale Pipeline Compression Experiment. A test pipe with a length of 8 m, a diameter of 1219 mm, a wall thickness of 26.4 mm, and a steel grade of X80 was installed on the mechanical loading platform. A driving arm and a confining arm were hinged to the pipe, and a hydraulic oil cylinder provided power to the driving arm with a movement of a constant velocity of 600 mm/min (Figure 4). Each movement was 20 mm, and each load was kept for more than 1 minute. The pipe hoop stress was generated by the constant internal water pressure. The axial stress was generated by the force resulting in tension strain in the outer side and compression strain in the inner side. Before the experiment, the welding of pipe flanges, installation of VWGs, and deployment of data acquisition system were completed. The trial operation included a pipe water pressure test, operation of hydraulic cylinder, data acquisition, and communication system test. The whole experiment took 1 hour and 9 minutes from loading to pipe rupture. Five monitoring sections in the test pipe were determined. For each monitoring section, five VWGs were installed at the 9, 10.5, 12, 13.5, and 3 o'clock positions, and one SG was installed at the 3 o'clock position for comparison (Figure 5).

2.3. Finite Element Simulation. The corresponding finite element model was established based on the experimental conditions with 332360 units and 381308 points (Figure 6). Five monitoring sections were also set in the same positions consistent with the experiment in the field. The x axis was along the driving arm direction, the y axis was along the vertical direction, and the z axis was along the pipe direction. In the model, zero displacement constraints in x, y, and z directions were applied to the restrained end, and zero displacement constraints in x and y directions were applied to the loading end. The hydraulic oil cylinder thrust applied an acting force on the nodes of the loading end in the form of a "concentrated force," while the internal water pressure stressed the nodes of the pipe inner wall in the form of a "uniform distribution force." The internal water pressure remained unchanged, and the force of oil cylinder thrust was the main load. The bolts in the field were ignored, and it is assumed that the driving arm and confining arm were directly connected with the pipe.

Under most geological conditions, pipelines are subjected to displacement load. Take frost heave displacement as an example; as illustrated in Figure 7, in the pipeline sections with frost-susceptible foundation soils and favorable hydrothermal conditions for frost heaving, the frost bulb generated by a cold pipeline may push the pipe upward while the adjacent pipes anchored in the frozen ground tend to hold the pipe down, causing bending of the pipe. If the bending strain becomes larger than the ultimate strain of the pipe, bucking or rupture failures of the pipe may happen. The pipe's loading condition was mainly simplified to a "concentrated force" applied by hydraulic oil cylinder thrust. The additional bending stress can be induced by the applied load in this way, and soil around the pipe was ignored. Although it is inconsistent with the field, the pipe's mechanical states can be reflected without considering the soil around the pipe at a lower cost.

3. Results

3.1. Distributions of Pipe Displacement and Stress. The variation in hydraulic oil cylinder thrust with time is shown in Figure 8. The oil cylinder provided power to the driving arm with a movement of a constant velocity of 600 mm/min. Each movement was 20 mm, and each load was kept for more than 1 minute. From 350 s to 1005 s, the load kept at 1577 kN, so it was observed that there was an obvious load stabilization stage during the loading process. The distributions of overall displacement, pipe displacement, and pipe stress at 651 s with cylinder thrust of 1577 kN and inner pressure of 10.9 MPa are shown in Figure 9. Under the movement of the driving arm, pipe axial stress values on the outer side were positive and the ones on the inner side were negative, illustrating that the outer side was tensile and the inner side was compressed. The displacements of each part of the pipe were distributed symmetrically along the pipe centerline in the z direction. The distributions of displacement and stress as well as symmetry were all under common sense. At the same time, the distributions of six stress components in the pipe are also given in Figure 10.

3.2. Verification of Results of FEM. According to the nonlinear FEM established, the calculated stress results of five pipe sections are listed in Table 1. All the maximum shear

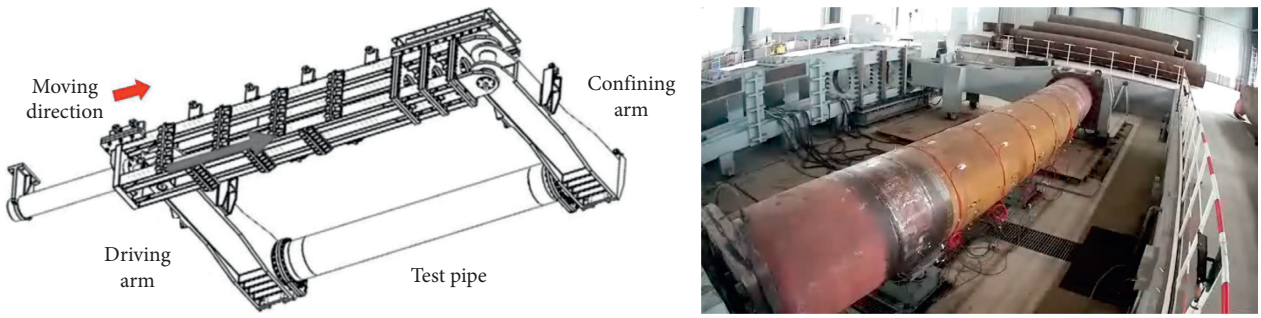

(a) (b)

Figure 4: Layout of large-scale pipe mechanical loading experiment: (a) schematic diagram; (b) site layout.

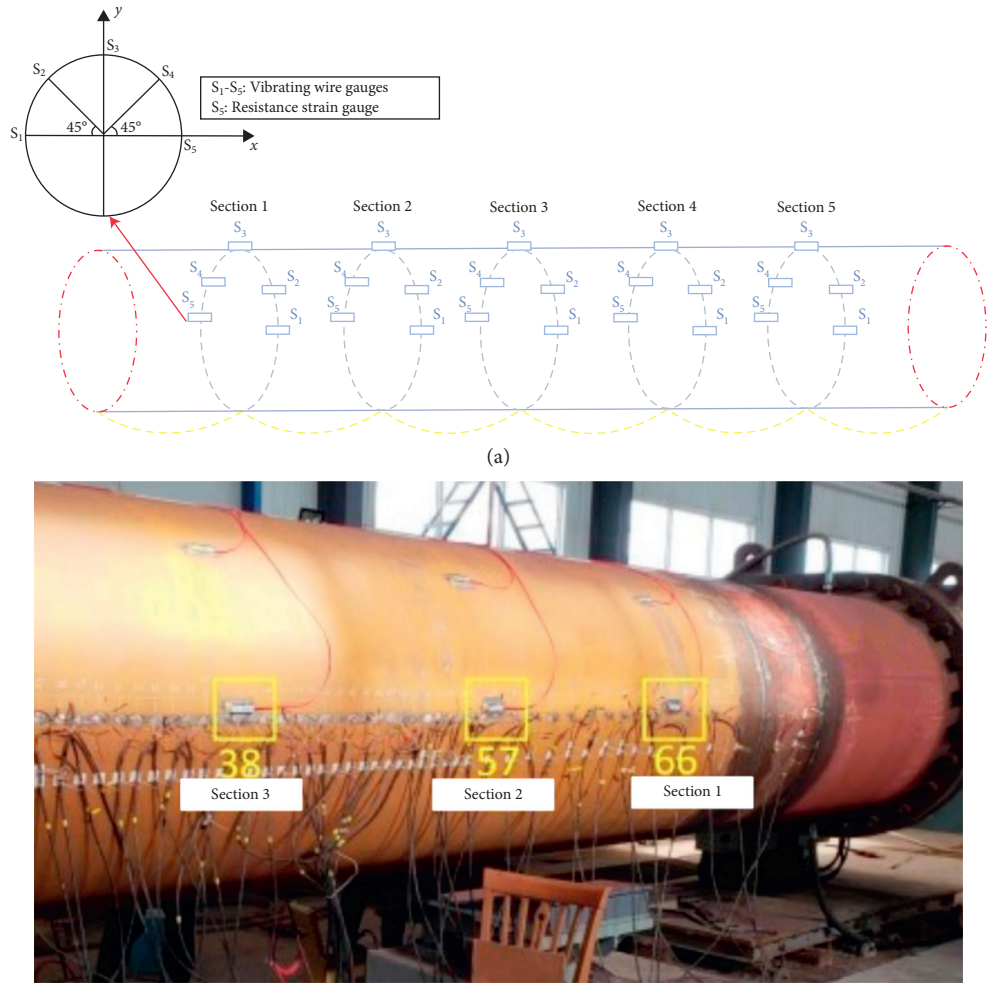

(a)

(b)

Figure 5: Arrangement of vibrating wire gauges and electrical resistance strain gauge: (a) schematic diagram; (b) site layout.

stresses in each section were less than 90% of pipe yield strength, illustrating that the pipe was in a linear elastic state. According to the basic theory of material mechanics, the results of FEM were compared with theoretical analysis (Table 2). The comparison results show the calculated values of the two methods were similar, and the maximum relative error was only 4.04%. Thus, the FEM was reliable and could be used to verify the effectiveness of the algorithm combined with the experiment results.

3.3. Comparison of Results between VWGs and SGs. The monitoring results of the VWGs installed at the 3 o'clock position in four pipe sections were compared with SGs

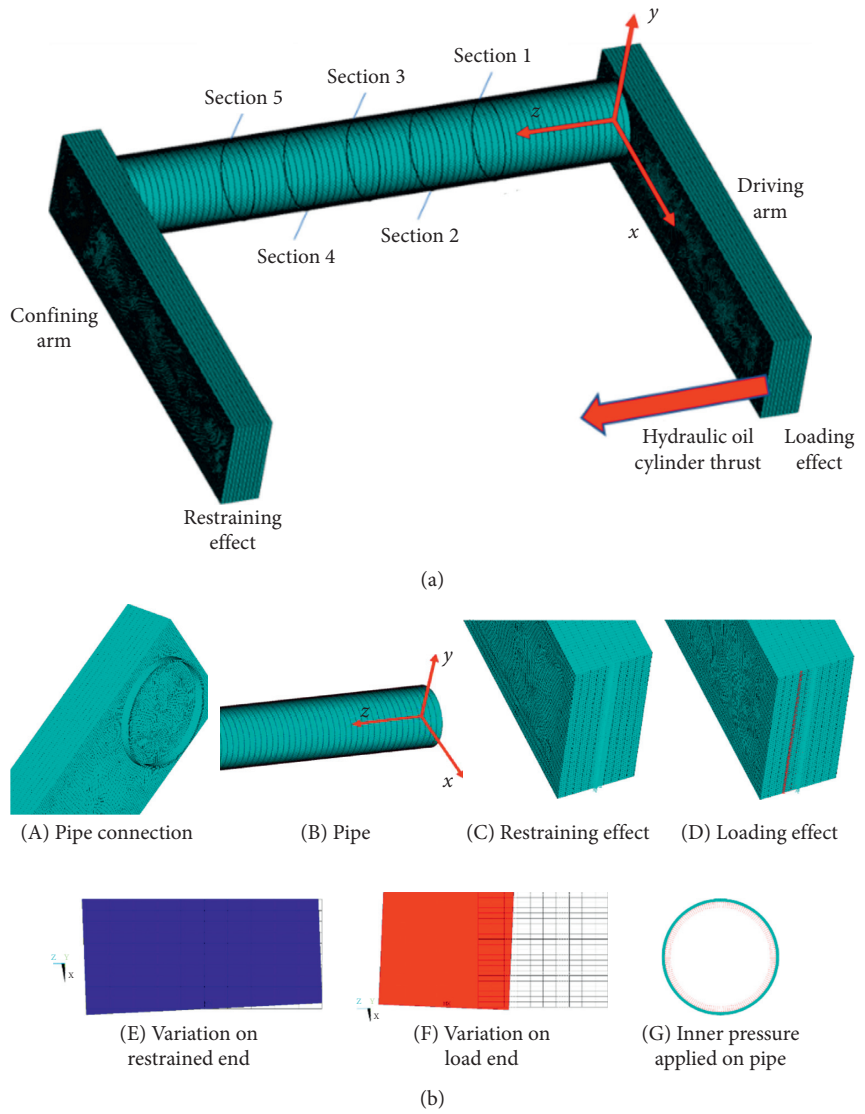

Figure 6: Finite element model established based on mechanical loading experiment: (a) overall model; (b) partial model.

which were located at the same positions (Figure 11). Since the monitoring results of section 1 were unreasonable, they were not used for analysis here. The comparison results show that there was a similar variation trend with a maximum relative error of 7.98% and a minimum of 1.19%. This illustrated that the VWGs were reliable in pipe axial strain monitoring with high relevance.

3.4. Optimization in Combination Modes of VWGs. According to the pipeline stress detection algorithm derived above, the maximum axial stress of the pipe section can be obtained by only knowing three axial strains. In this experiment, there were 5 VWGs arranged on each pipe section, so there were 10 different combination modes in total if 3 were selected for one combination. To evaluate the reliability of the algorithm and optimize the combination modes of VWGs, the results of 10 different combination modes in 5 monitoring sections were substituted into the algorithm to compute the stress for comparison with the FEM results. Take pipe section 1 as an example; the comparison of results between stress algorithm and FEM are listed in Table 3. Before the screening, the relative error of the shear stress was −13.33~48.11%.

As can be seen from Figure 12, when the combination modes from the first to the sixth were adopted, the relative error of the maximum axial stress ranged from −7.79 to 26.74%. Among all sections, the error of section 4 was relatively small, ranging from −0.48 to 2.82%, and the minimum error was −0.09%. When the third, fifth, sixth, eighth, ninth, and tenth combination modes were adopted, the relative error of the minimum axial stress ranged from −6.00 to 31.48%, and the error of section 4 was relatively small, with a minimum value of −6.00%. The relative error of the maximum shear stress ranged from −13.26 to 14.59% when the second to the sixth combination modes were used. Among all sections, the error of section 5 was relatively small, ranging from −1.46 to 0.72%, and the minimum error

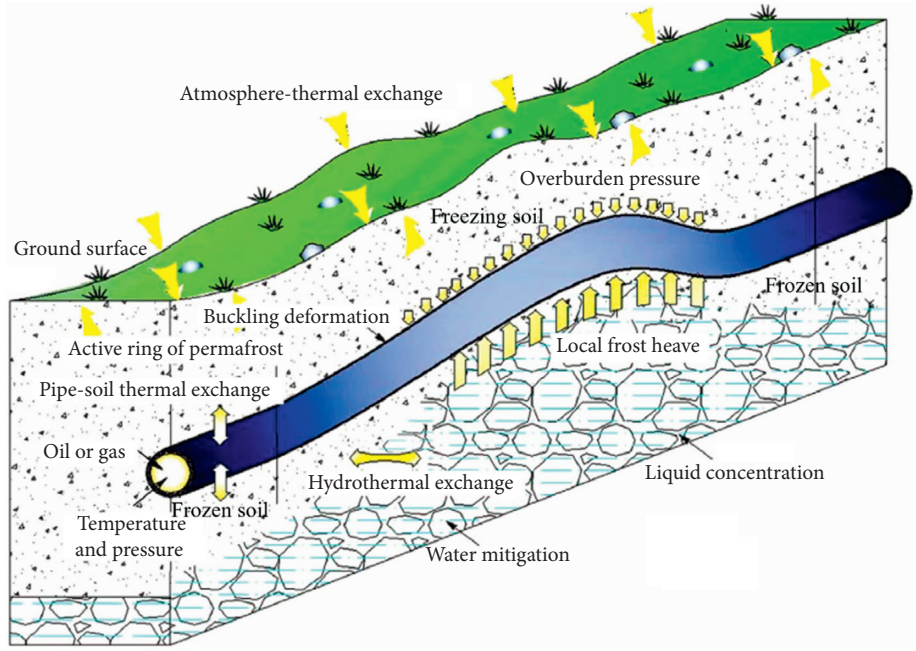

Figure 7: Schematic of pipeline subjected to frost heave displacement load [31].

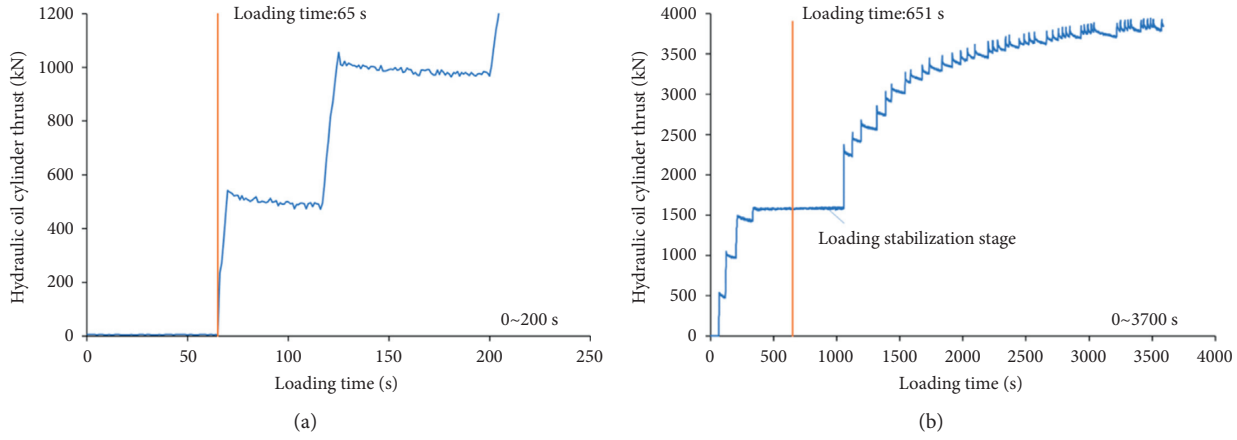

Figure 8: Variation in hydraulic oil cylinder thrust with time: (a) 0~200 s; (b) 0~3700 s.

was 0.34%. It is important to note that in the stress analysis of a pipeline, the strength check is mainly judged by the maximum shear stress, and the maximum and minimum axial stress are only the intermediate results of the pipeline stress detection algorithm. Thus, the optimal combination modes for the maximum shear stress should be adopted to evaluate pipe safety. Based on the comparison of VWGs monitoring results and FEM simulation results, the error of gauging point S_3 was large. The reason is that gauging point S_3 is located near the neutral axis. Under the same load condition, the monitoring strain value of this point is much smaller than those of other points (S_1, S_2, S_4, S_5), which easily causes large errors. Therefore, the curve fluctuates up and down when combination modes including gauging point S_3 are plotted.

4. Discussion

According to the basic theory of material mechanics, under the condition of linear elasticity and small deformation, the strain obeys the assumption of a plane section, so the results of measuring points S_1~S_5 in the same section should present a straight line in the ideal state. The monitoring results of five sections could be drawn in one figure (Figure 13(a)). If a measuring point deviated too far from the straight line, this indicated that it was not reliable and should be excluded. In addition, when the force applied on multiple sections was similar, the measuring points of each section should be approximately collinear in the ideal state (Figure 13(b)). If the straight line of one section deviated too

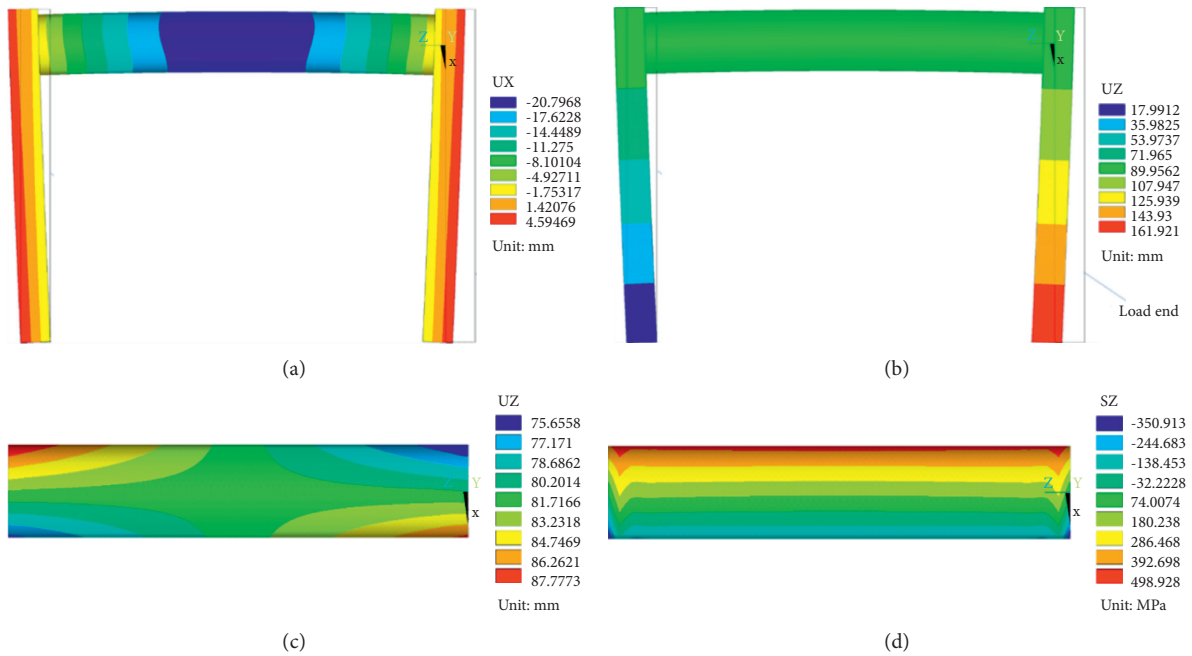

Figure 9: Distributions of overall displacement, pipe displacement, and pipe stress at 651 s: (a) distribution of overall displacement in x direction; (b) distribution of overall displacement in z direction; (c) distribution of pipe displacement in z direction; (d) distribution of pipe axial stress in z direction.

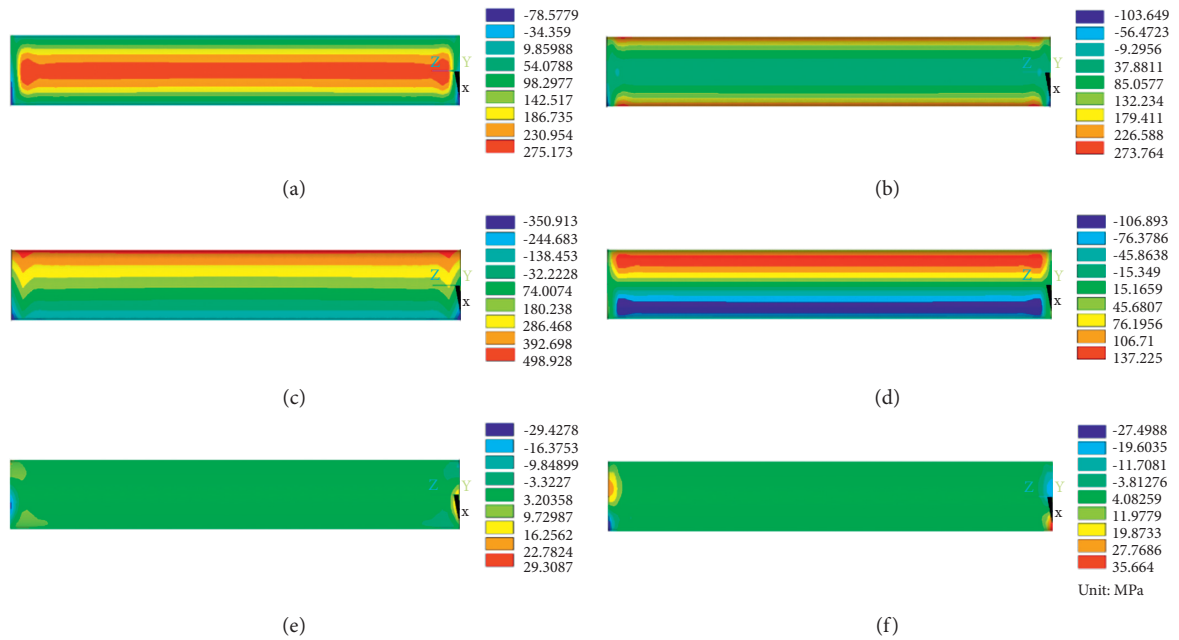

Figure 10: Distributions of six stress components in the pipe at 651 s: (a) pipe stress σ_x; (b) pipe stress σ_y; (c) pipe stress σ_z; (d) pipe stress τ_{xy}; (e) pipe stress τ_{yz}; (f) pipe stress τ_{xz}.

far, this indicated that the monitoring result of this section was not reliable and should be excluded.

Take the strain results of pipe section 1 as an example. Firstly, the fitting line was drawn utilizing the least square method (Figure 14). Then, the distance from each point to the line was squared, and the point with the greatest deviation was gotten rid of. It was S_4 in this case. After the S_4 was excluded, the initial ten combination modes could be reduced to four combination modes. Finally, the results of the remaining points, S_1, S_2, S_3, and S_5, were substituted into the algorithm to compute the stress values of the four combination modes. The relative error of maximum shear stress could be reduced from −13.33~48.11% to −13.33~2.26%. With the same method, the results of S_2 in

Table 1: Calculated stress results of FEM in five pipe sections.

Section	Maximum/minimum axial stress σ_L (MPa)		Hoop stress σ_h (MPa)	Equivalent stress (MPa)		Maximum shear stress τ_{max} (MPa)	90% of yield strength $0.9\sigma_s$ (MPa)
	σ_{max}	σ_{min}		$\sigma_h - \sigma_{max}$	$\sigma_h - \sigma_{min}$		
1	423.05	−232.48	252.37	−170.68	484.85	484.85	499.50
2	427.33	−228.31	252.37	−174.96	480.68	480.68	499.50
3	428.86	−227.02	252.37	−176.49	479.39	479.39	499.50
4	427.32	−228.31	252.37	−174.95	480.68	480.68	499.50
5	423.04	−232.49	252.37	−170.67	484.86	484.86	499.50

Table 2: Comparison results between FEM and theoretical analysis.

Section	Maximum axial stress σ_{max} (MPa)			Minimum axial stress σ_{min} (MPa)		
	FEM	Material mechanics	Relative error	FEM	Material mechanics	Relative error
1	423.05	432.28	−2.13%	−232.48	−223.45	−4.04%
2	427.33	432.28	−1.14%	−228.31	−223.45	−2.17%
3	428.86	432.28	−0.79%	−227.02	−223.45	−1.60%
4	427.32	432.28	−1.15%	−228.31	−223.45	−2.17%
5	423.04	432.28	−2.14%	−232.49	−223.45	−4.04%

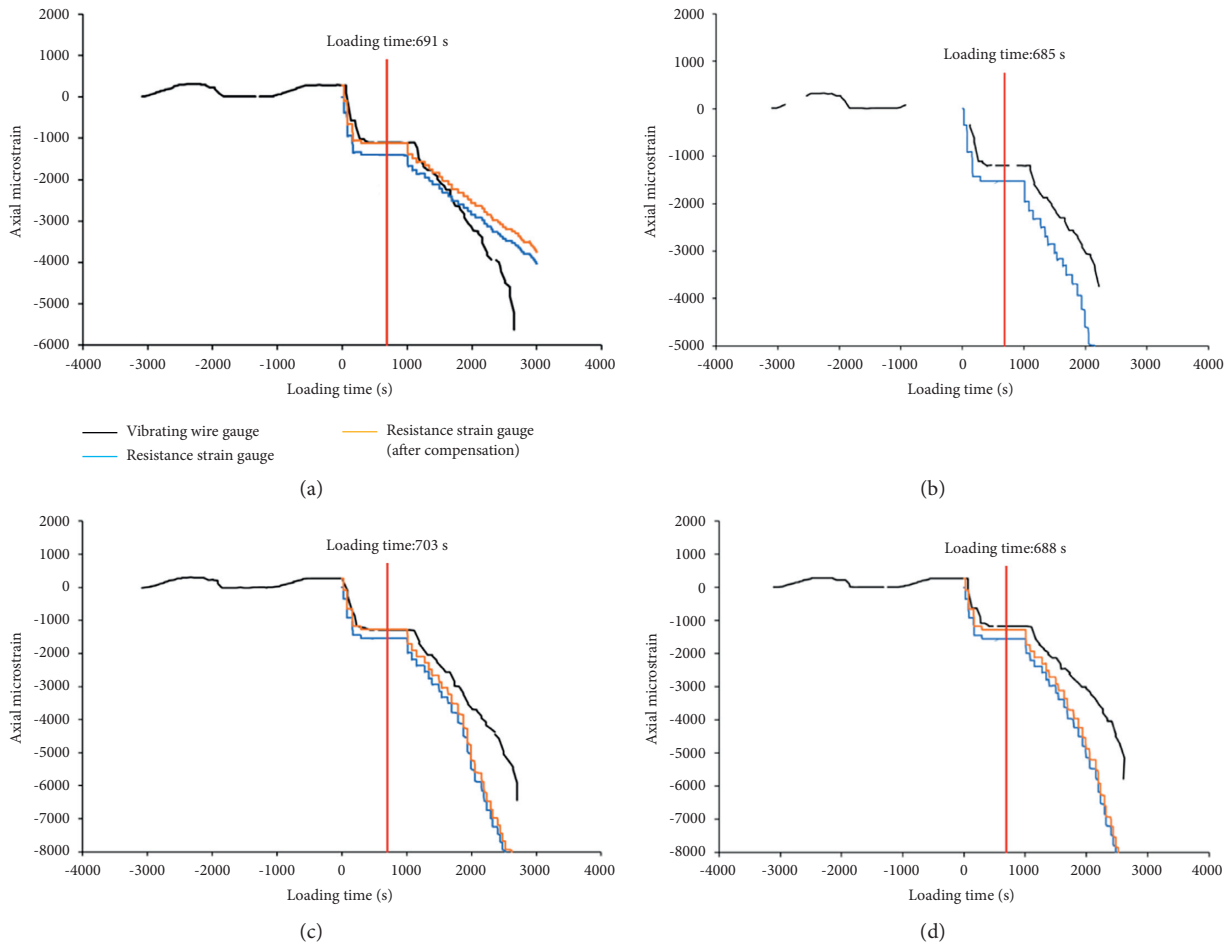

Figure 11: Comparison of results between VWGs and SGs (the red vertical line stands for the loading time): (a) section 2; (b) section 3; (c) section 4; (d) section 5.

Table 3: Comparison of results between stress algorithm and FEM in pipe section 1.

No.	Combination modes			Maximum axial stress σ_{max} (MPa)			Minimum axial stress σ_{min} (MPa)			Maximum shear stress τ_{max} (MPa)		
				Algorithm	FEM	Relative error	Algorithm	FEM	Relative error	Algorithm	FEM	Relative error
1	S_1	S_2	S_3	393.71	423.05	−6.93%	−245.18	−232.48	−5.46%	497.55	484.85	2.62%
2	S_1	S_2	S_4	394.74	423.05	−6.69%	−284.02	−232.48	−22.17%	536.39	484.85	10.63%
3	S_1	S_2	S_5	391.94	423.05	−7.35%	−170.02	−232.48	26.87%	422.39	484.85	−12.88%
4	S_1	S_3	S_4	398.27	423.05	−5.86%	−303.21	−232.48	−30.42%	555.58	484.85	14.59%
5	S_1	S_3	S_5	390.10	423.05	−7.79%	−168.17	−232.48	27.66%	420.55	484.85	−13.26%
6	S_1	S_4	S_5	400.07	423.05	−5.43%	−178.15	−232.48	23.37%	430.52	484.85	−11.21%
7	S_2	S_3	S_4	376.44	423.05	−11.02%	−319.19	−232.48	−37.30%	571.56	484.85	17.88%
8	S_2	S_3	S_5	420.19	423.05	−0.68%	−167.86	−232.48	27.79%	420.24	484.85	−13.33%
9	S_2	S_4	S_5	515.46	423.05	21.84%	−182.34	−232.48	21.57%	515.46	484.85	6.31%
10	S_3	S_4	S_5	718.14	423.05	69.75%	−189.94	−232.48	18.30%	718.14	484.85	48.11%

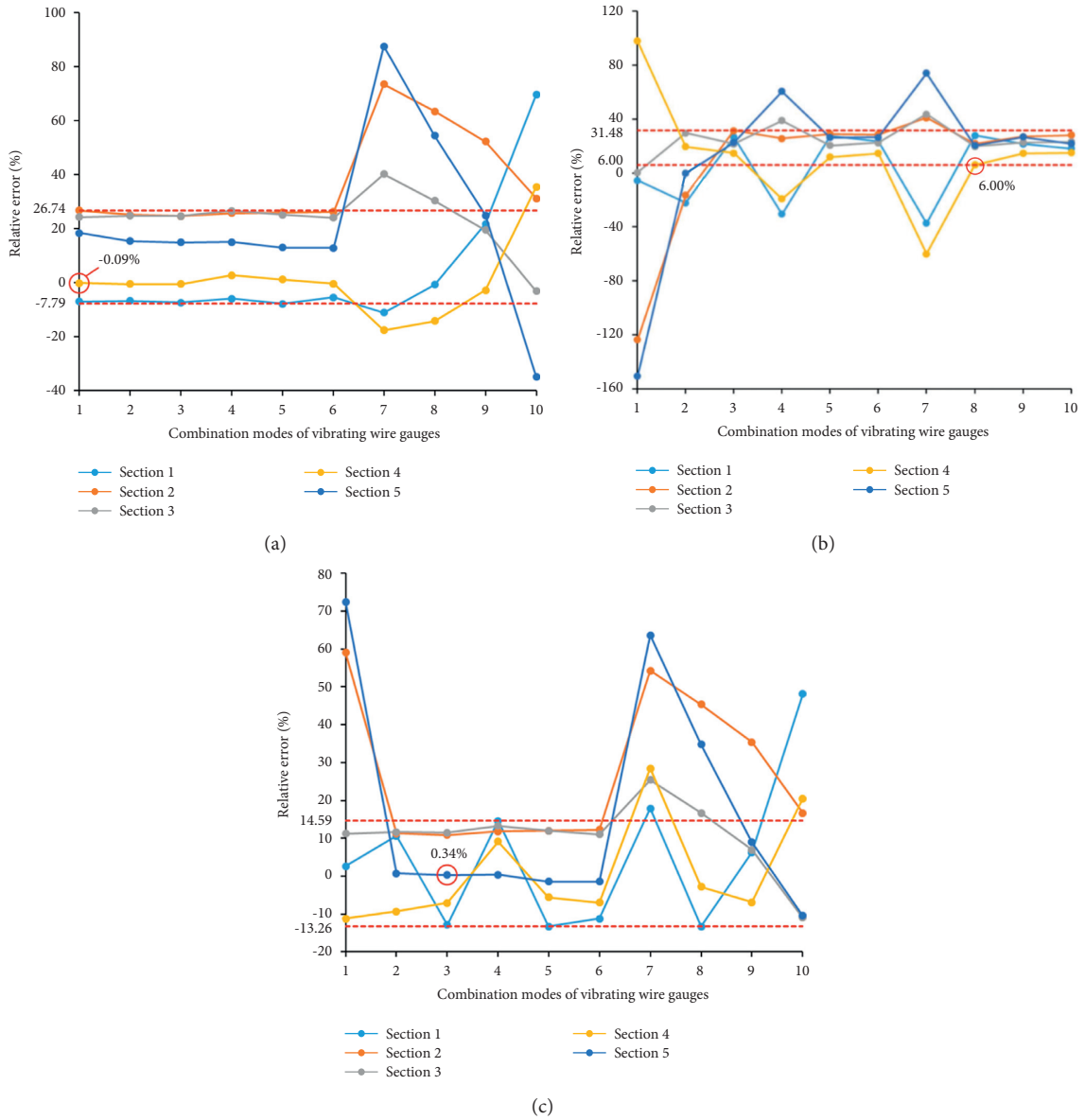

Figure 12: Comparison of results between algorithm and FEM: (a) maximum axial stress σ_{max}; (b) minimum axial stress σ_{min}; (c) maximum shear stress τ_{max}.

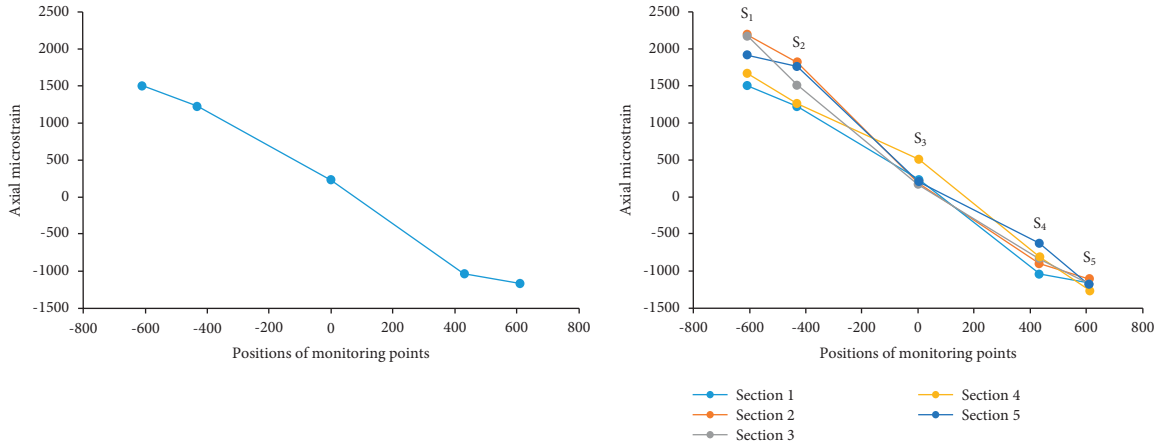

Figure 13: Monitoring results of VWGs: (a) pipe section 1; (b) pipe sections 1~5.

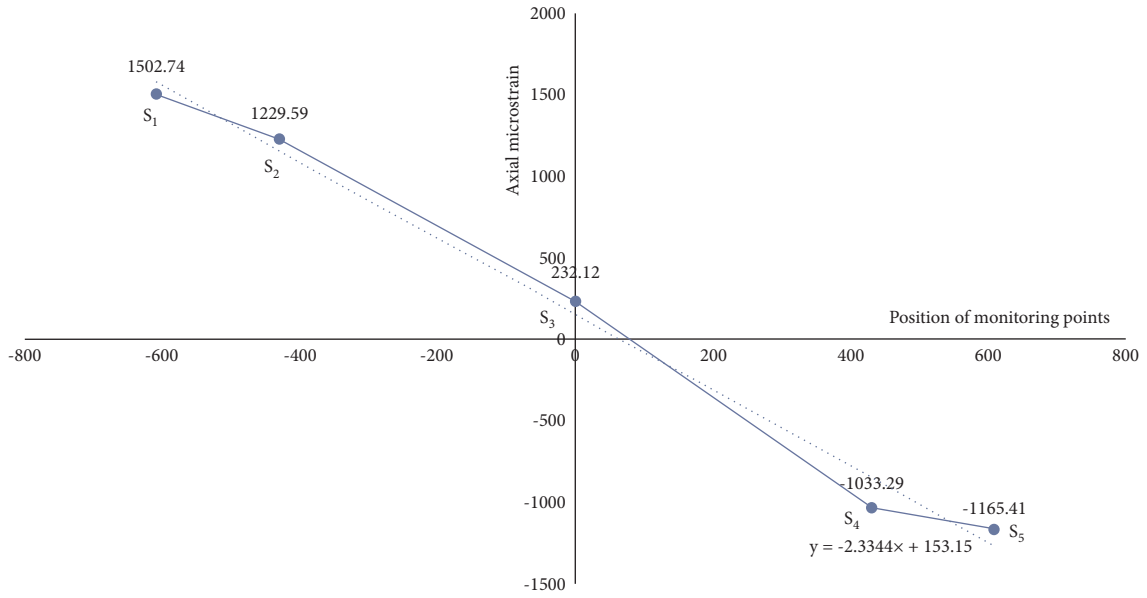

Figure 14: Trend line fitted by 5 monitoring points in pipe section 1 utilizing the least square method.

section 2 and S_3 in sections 3~5 deviated from the fitting line and were not substituted into the algorithm in calculating the stress. The relative errors of the maximum shear stress in sections 2~5 were further reduced to 11.82~16.66%, 6.94~11.66%, −9.32~6.9%, and −1.46~8.99%, respectively. The overall relative error of the five sections was determined as −13.33~16.66% which was similar to −13.26~14.59% presented initially above.

In addition, when the error was negative, it indicated that the calculation result of the algorithm was smaller compared with the real condition. On the contrary, a positive value means that it was larger. The former will lead to pipe strength warning with a delay, which may cause engineering accidents. The latter will cause the warning to be too sensitive, resulting in wasting the bearing capacity of the pipe. However, the former consequence was more serious.

5. Conclusions

(1) According to the theory of material mechanics and Hook's Law, a pipe stress detection algorithm, which could compute the maximum axial stress by only knowing three axial strains of the pipe section, was derived.

(2) To verify the effectiveness of the stress detection algorithm, a large-scale pipeline compression experiment was conducted on a mechanical loading platform, and a corresponding FEM was established. The VWGs were reliable in pipe axial strain monitoring compared with SGs attached at the same location with a relative error of 1.19%~7.98%. The FEM was also credible compared with theoretical analysis with a maximum relative error of 4.04%.

Thus, the algorithm could be verified by the experiment combined with the FEM.

(3) The least square method could be utilized in excluding unreliable monitoring points of VWGs, and combination mode numbers could be reduced from 10 to 4. When the reasonable combination modes of VWGs were chosen, the error of the pipeline stress detection algorithm could be controlled within a range of −13.33~16.66% with enough accuracy for engineering application.

(4) Limited by measuring accuracy of VWGs, the measuring point at pipe crown is not recommended to be arranged because this measuring point is easy to cause a large measuring error.

Data Availability

The data used to support the findings of this study are available from the corresponding author upon request.

Conflicts of Interest

The authors declare no conflicts of interest.

Acknowledgments

This research was funded by the Chinese Academy of Sciences (CAS) Strategic Priority Research Program (Grant no. XDA20100103).

References

[1] M. C. Brewer, H. J. Jin, W. Z. Hu, X. J. Zhang, and J. F. Chen, "The changes of design of the Alyeska pipeline and construction modes in permafrost areas, and their reasons and the philosophy behind it," *Journal of Glaciology and Geocryology*, vol. 28, no. 6, pp. 809–817, 2006.

[2] R. L. Wang and Y. H. Yeh, "A refined seismic analysis and design of buried pipeline for fault movement," *Earthquake Engineering & Structural Dynamics*, vol. 13, no. 1, pp. 75–96, 1985.

[3] Y. P. Wu, Y. Sheng, Y. Wang, H. J. Jin, and W. Chen, "Stresses and deformations in a buried oil pipeline subject to differential frost heave in permafrost regions," *Cold Regions Science and Technology*, vol. 64, no. 3, pp. 256–261, 2010.

[4] B. X. Yuan, Z. H. Li, Z. L. Su, Q. Z. Luo, M. J. Chen, and Z. Q. Zhao, "Sensitivity of multistage fill slope based on finite element model," *Advances in Civil Engineering*, vol. 2021, Article ID 6622936, 13 pages, 2021.

[5] B. Bai, Q. K. Nie, Y. K. Zhang, X. L. Wang, and W. Hu, "Cotransport of heavy metals and SiO2 particles at different temperatures by seepage," *Journal of Hydrology*, vol. 597, Article ID 125771, 2021.

[6] E. L. Liu and Y. M. Lai, "Thermo-poromechanics-based viscoplastic damage constitutive model for saturated frozen soil," *International Journal of Plasticity*, vol. 128, Article ID 102683, 2020.

[7] A. Gens, "Soil-environment interactions in geotechnical engineering," *Géotechnique*, vol. 60, no. 1, pp. 3–74, 2010.

[8] B. Bai, G. C. Yang, T. Li, and G. S. Yang, "A thermodynamic constitutive model with temperature effect based on rearrangement for geomaterials," *Mechanics of Materials*, vol. 139, Article ID 103180, 2019.

[9] B. Bai, R. Zhou, G. Q. Cai, W. Hu, and G. C. Yang, "Coupled thermo-hydro-mechanical mechanism in view of the soil particle rearrangement of granular thermodynamics," *Computers and Geotechnics*, vol. 137, no. 8, Article ID 104272, 2021.

[10] B. Liu, X. J. Liu, and H. Zhang, "Strain-based design criteria of pipelines," *Journal of Loss Prevention in the Process Industries*, vol. 22, no. 6, pp. 884–888, 2009.

[11] C. P. Ellinas, "Pipeline design based on strain criteria," *Chemical Business*, vol. 13, no. 5, pp. 131–135, 1999.

[12] J. W. Wilson, G. Y. Tian, and S. Barrans, "Residual magnetic field sensing for stress measurement," *Sensors and Actuators A: Physical*, vol. 135, no. 2, pp. 381–387, 2007.

[13] L. Huang, Y. Sheng, J. C. Wu, W. Cao, E. X. Peng, and X. Y. Zhang, "Experimental study on mechanical interaction between buried pipe and soil during freezing," *Cold Regions Science and Technology*, vol. 178, Article ID 103129, 2020.

[14] N. S. Rossini, M. Dassisti, K. Y. Benyonnis, and A. G. Olabi, "Methods of measuring residual stresses in components," *Materials & Design*, vol. 119, no. 35, pp. 572–588, 2011.

[15] W. Y. Kuang, "Numerical study of strain-based monitoring parameter on steel strip reinforced thermoplastic pipe (SSRTP) under internal pressure," *Journal of Pipeline Science and Engineering*, vol. 1, no. 2, pp. 233–240, 2021.

[16] S. A. Suhail, M. Danish, A. A. Sheikh, and A. Nawaz, "Monitoring pile performance using fiber optic sensor technology-an account on recent developments," in *Proceedings of the International Conference on New Challenges In Geotechncial Engineering*, Lahore, Pakistan, January 2017.

[17] B. X. Yuan, Z. H. Li, Z. Q. Zhao, H. Ni, Z. L. Su, and Z. J. Li, "Experimental study of displacement field of layered soils surrounding laterally loaded pile based on transparent soil," *Journal of Soils and Sediments*, vol. 21, no. 9, pp. 3072–3083, 2021.

[18] P. P. Yang, N. Q. Wang, Z. Y. Jiang, Y. Yang, and H. P. Yan, "Overview of slope monitoring technology," *IOP Conference Series: Materials Science and Engineering*, vol. 472, Article ID 012009, 2019.

[19] B. X. Yuan, Z. H. Li, Y. M. Chen et al., "Mechanical and microstructural properties of recycling granite residual soil reinforced with glass fiber and liquid-modified polyvinyl alcohol polymer," *Chemosphere*, vol. 286, Article ID 131652, 2021.

[20] J. M. Oswell, "Pipelines in permafrost: geotechnical issues and lessons," *Canadian Geotechnical Journal*, vol. 48, no. 9, pp. 1412–1431, 2011.

[21] R. M. Doblanko, J. M. Oswell, and A. J. Hanna, "Right-of-way and pipeline monitoring in permafrost: the Norman Wells pipeline experience," in *Proceedings of the 4th International Pipeline Conference*, pp. 605–614, Calgary, Alberta, Canada, September 2002.

[22] H. M. Wei, C. Y. Tao, Y. N. Zhu, and S. Krishnaswamy, "Fiber Bragg grating dynamic strain sensor using an adaptive reflective semiconductor optical amplifier source," *Applied Optics*, vol. 55, no. 10, p. 2752, 2016.

[23] S. Villalba and J. R. Casas, "Application of optical fiber distributed sensing to health monitoring of concrete structures," *Mechanical Systems and Signal Processing*, vol. 39, no. 12, pp. 441–451, 2013.

[24] H. J. Yoon, K. W. Song, H. M. Kim, and J. S. Kim, "Strain monitoring of composite steel girder bridge using distributed

optical fibre sensor system," *Procedia Engineering*, vol. 10, no. 7, pp. 2544–2547, 2011.

[25] L. L. K. Cheung, K. Soga, Y. Bennett, P. J. Kobayashi, B. Amatya, and P. Wright, "Optical fibre strain measurement for tunnel lining monitoring," *Geotechnical Engineering*, vol. 163, no. 3, pp. 119–130, 2010.

[26] M. M. Burgess and D. G. Harry, "Norman Wells pipeline permafrost and terrain monitoring: geothermal and geomorphic observations, 1984-1987," *Canadian Geotechnical Journal*, vol. 27, no. 2, pp. 233–244, 1990.

[27] C. L. Jiang, P. C. Chen, R. Li, and X. B. Liu, "A multisource monitoring data coupling analysis method for stress states of oil pipelines under permafrost thawing settlement load," *Mathematical Problems in Engineering*, vol. 2020, pp. 1–15, Article ID 6696680, 2020.

[28] P. Wang, Y. L. Gao, G. Y. Tian, and H. T. Wang, "Velocity effect analysis of dynamic magnetization in high speed magnetic flux leakage inspection," *NDT & E International*, vol. 64, pp. 7–12, 2014.

[29] C. Borda, M. Niklès, E. Rochat, A. Grechanov, A. Naumov, and V. Velikodnev, "Continuous real-time pipeline deformation, 3D positioning and ground movement monitoring along the Sakhalin-Khabarovsk-Vladivostok pipeline," in *Proceedings of the International Pipeline Conference*, vol. 45134, pp. 179–187, September 2012.

[30] F. Ravet, E. G. Ortiz, B. Peterson, and G. Hoglund, "Geohazard prevention with online continuous fiber optic monitoring," in *Proceedings of the Rio Pipeline Conference and Exposition*, Rio de Janeiro, Brazil, September 2011.

[31] L. Huang, Y. Sheng, X. Y. Hu, and S. T. Wang, "Interactions between the pipeline and soils in permafrost regions: a review," *Journal of Glaciology and Geocryology*, vol. 39, no. 1, pp. 112–122, 2017, in Chinese.